Journal of Colloid and Interface Science 613 (2022) 720–732

Contents lists available at ScienceDirect

Journal of Colloid and Interface Science

journal homepage: www.elsevier.com/locate/jcis

Binder free cobalt iron phosphate thin films as efficient electrocatalysts for overall water splitting

Suraj A. Khalate [a], Sujit A. Kadam [b], Yuan-Ron Ma [b], Sachin B. Kulkarni [c], Vinayak G. Parale [d], Umakant M. Patil [a,*]

[a] Centre for Interdisciplinary Research (CIR), D. Y. Patil Education Society, Kolhapur-416006, India
[b] Department of Physics, National Dong Hwa University, Hualien-97401, Taiwan
[c] Department of Physics, Tuljaram Chaturchand College, Baramati-413102, India
[d] Department of Materials Science and Engineering, Yonsei University, 50 Yonsei-ro, Seodaemun-gu, Seoul-03722, Republic of Korea

GRAPHICAL ABSTRACT

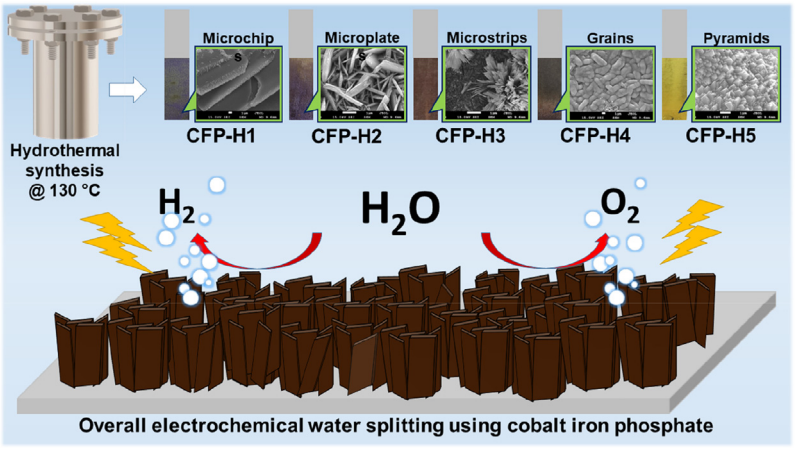

ARTICLE INFO

Article history:
Received 12 October 2021
Revised 22 December 2021
Accepted 3 January 2022
Available online 12 January 2022

Keywords:
Composition
Hydrothermal synthesis
Morphological evolution
Overall water splitting
Synergistic effect

ABSTRACT

Designing nanostructure based robust catalyst for the electrochemical water splitting is the great task in the energy conversion field to accomplish high electrical conductivity, low overpotential and long lasting activity. Herein, the electrochemical overall water splitting is reported by using the hydrothermally synthesized binder free cobalt iron phosphate thin films on low cost stainless steel substrates as a conducting backbone for the first time. The effect of composition ratio variation of cobalt and iron was studied on the structural, compositional, morphological, and surface electronic properties by conducting various characterizations which results in amorphous hydrous cobalt iron phosphate having mesoporosity. The as synthesized cobalt iron phosphate having composition ratio (50:50 of Co:Fe) exhibits excellent electrochemical OER and HER catalytic water splitting performance. Best performing electrode exhibits smallest overpotentials of 251.9 mV and 55.5 mV for OER and HER respectively at 10 mA/cm^2 current density. To split water molecule into the H_2 and O_2 by overall water splitting in same alkaline medium,

* Corresponding author.
E-mail address: umakant.physics84@gmail.com (U.M. Patil).

https://doi.org/10.1016/j.jcis.2022.01.015

the potential of 1.75 V was required after long duration (100 h) catalysis. Overall analysis confirms the cobalt iron phosphate thin films are outstanding and robust for the hydrogen production as clean renewable energy source.

1. Introduction

With the increase in demand of the energy, there is need to increase the sources to generate it to fulfil our requirements. Fossil fuels have biggest share in the energy generation in which coal, gas and oil are prominent. These nonrenewable sources make serious impact by emitting CO_2 and other hazardous gases which pollute our benign environment [1–3]. Today, there is need to produce energy from green and sustainable resources to avoid future crisis, global warming and environmental pollution. It is interesting thing that, there is rapid transition from non-renewable sources to the renewable [4]. Solar, wind, hydrodynamic, etc. are popular renewable sources. Hydrogen is one of the source which has high potential to change the situation of energy demand and generation in a future sustainable sector [5]. There are enormous techniques to produce hydrogen, from which splitting of water by the application of electricity (electrochemical) or solar radiation (Photochemical) or electricity and solar radiation (photoelectrochemical) are effective ways [6,7]. Electrochemical water splitting is an effective technique to convert electrical energy into chemical in the form of hydrogen with the help of proper catalyst electrode. Electrochemical water splitting is the combination of two half-reactions as hydrogen evolution reaction (HER) on the cathode and oxygen evolution reaction (OER) on the anode. But these reactions are not thermodynamically favorable. The theoretical potential needed to initiate water splitting is 1.23 V. Practically we need to supply some additional potential (called as overpotential) more than the theoretical value due to the energy losses during energy conversion [8,9]. Electrocatalysts play an important role in minimizing the overpotential by providing active sites, easy charge transfer, and high ion adsorption energy. To diminish the overpotential and energy wastage during OER, there are some requirements of a worthy electrocatalyst such as, high catalytic activity, greater electrical conductivity, easy mass transport, unperturbed gas release and satisfactory electrocatalytic stability [10].

At present, the state-of-the-art materials like platinum, ruthenium/iridium and their oxides are extensively applied as the best electrocatalysts with high efficiency [11–13]. But, because of their inadequacy, expensiveness, high overpotentials for large current densities and deprived stability, the marketable usage of these precious materials is not possible [14–17]. Many alternatives to the noble metal catalysts have been discovered to minimize the cost of catalyst material. Among the all non-noble electrocatalysts, compounds of the first row 3d-orbital transition metals such as oxides, hydroxides, nitrides, phosphides, phosphates, chalcogenides, borides, etc. are highly attractive because of the superficial conversion of their oxidation states, low cost and relatively high activity [18–24]. Transition metal phosphate catalysts are promising for electrochemical water splitting who provides adsorption and alleviating active sites. Moreover, simultaneously phosphate ligands contribute the advantageous situations for electrolyte ion adsorption and oxidation by disturbing native atomic configuration. The phosphate ligands enable the oxidation of metal atoms at the time of proton coupled electron transfer [10]. Cobalt iron phosphate is one of the promising material for the water oxidation. According to previous reports, it is clear that, amorphous materials are electrochemically more active than well crystalline materials synthesized at higher temperature, by the reason of huge number of coordinatively unsaturated sites and surface defects. Liu et. al. [25] synthesized cross linked porous cobalt-iron pyrophosphate by co-precipitation method which showed overpotential of 276 mV at 10 mA/cm^2 current density and around 30000 s (8.33 h) OER stability. Tremella-like cobalt iron phosphate nanosheets synthesized via microwave-assisted precipitation, which delivered 94 % current density retention at constant water oxidation with overpotential 267 mV at 10 mA/cm^2 current density [26]. These reports revealed that there were powder coating techniques used for the preparation of catalyst electrodes. It is worth noting that, there is only a report of direct growth (binder free) cobalt iron phosphate on Ni-foam for HER study [27]. Nickel foam offers excellent conductivity as a substrate but itself shows catalytic behavior in alkaline electrolyte. Cobalt doped iron phosphate was synthesized and studied electrochemical water splitting by our group [28]. At the doping concentration of 2.01 At%, low overpotentials (266 mV for OER, 82.3 mV for HER and 2.04 V for overall water splitting) were recorded. It is observed that, due to the limitations in doping, there is limited increment in electrochemical performance. On the other hand, it is advantageous to prepare the composition of cobalt and iron in their proportion for the novel morphology and the synergistic effect during electrochemical processes. Still there is no any report for OER, HER and overall water splitting by using cobalt iron phosphate thin films directly deposited (binder free) on stainless steel (SS) substrates.

Herein, for the first time, binder free cobalt iron phosphate thin films were synthesized on SS substrate via single step hydrothermal approach. As compared to other substrates like Ni-foam or carbon cloth, SS substrates have low cost, easy availability, high electrical conductivity and most importantly the non-reactivity in acidic or alkaline media. In the present work, the morphological evolution due to change in compositional ratio of cobalt and iron, and their effect on the electrochemical OER, HER, and overall water splitting is studied. The synergistic effect, amorphous nature, mesoporosity, submicrometric strips like morphology and the transition to the higher electronic states of metals during catalysis are witnessing the enhancement in electrochemical catalytic water splitting process.

2. Experimental section

2.1. Materials used and substrate cleaning

For the preparation of cobalt-iron phosphate, the analytical grade chemicals were used as $CoCl_2{\cdot}6H_2O$, $FeCl_2$, KH_2PO_4, and urea ($CO(NH_2)_2$) purchased from Sigma-Aldrich. The as-purchased chemicals were used for catalyst synthesis without further purification. Before the preparation for reaction, SS substrates were systematically washed. The 1 cm × 6 cm pieces of SS were polished by very fine zero grade polish paper and rinsed with laboratory soap solution and double distilled water (DDW) severally. After wash, substrates were transferred to the solution of ethanol and water and ultrasonicated for 20 min.

2.2. Synthesis of cobalt iron phosphate thin films

A facile and binder free hydrothermal method was used to synthesize cobalt iron phosphate thin film electrodes on SS substrates.

The solutions were prepared separately in 50 ml double distilled water by dissolving 0.1 *M* KH_2PO_4, 0.1 *M* urea and the mole percent ratio was varied for $CoCl_2{\cdot}6H_2O$ and $FeCl_2$. The prepared individual solutions were mixed together and stirred at room temperature for 30 min to became it homogenous. After stirring, the solutions were transferred to Teflon lined SS hydrothermal bombs. The thoroughly cleaned SS substrates were kept vertically in the solutions and the bombs were sealed tightly. Hydrothermal bombs were then kept in laboratory oven and temperature maintained at 130 °C for 14 h. After completing the reaction time, the reactions allow to cool naturally and the films were removed, washed by means of double distilled water twice to remove loosely bonded material particles and dried in ambient temperature. The synthesized cobalt iron phosphate thin films were named as CFP-H2, CFP-H3 and CFP-H4 for the ratios of Co:Fe as 75:25, 50:50 and 25:75, respectively. For comparison, the cobalt phosphate was prepared by keeping ratio of Co:Fe as 100:0 named as CFP-H1 and the iron phosphate was prepared by keeping ratio of Co:Fe as 0:100 named as CFP-H5.

2.3. Characterizations

From Rigaku Miniflex 600 X-ray diffractometer using Cu-Kα target radiation (λ = 1.5406 Å), the XRD patterns of the materials were collected in 2θ range from 5 to 80°. Molecular vibrational analysis was performed by FTIR spectroscopy using alpha (II) Bruker spectroscope in the wavenumber range 400 to 4000 /cm. XPS conducted for electronic state information using X-ray photoelectron spectrometer (XPS, Thermo Scientific Inc. K-alpha) having microfocus monochromatic radiations of Al Kα X-ray. Compositional and surface morphological characteristics were carried by EDS and Field Emission Scanning Electron Microscopy by FESEM, JEOL JSM-6500F. The surface analysis was carried by Belsorp II mini via N_2 adsorption–desorption isotherms.

2.4. Electrochemical characterizations

Entire electrochemical characteristics carried on ZIVE MP1 electrochemical workstation using typical three electrodes electrochemical cell configuration. The as-deposited samples and platinum strip act as a working and counter electrodes. As a reference, saturated calomel electrode (SCE) was used. The OER was studied in 1 *M* KOH having pH equals to 13.7 and HER in 1 *M* H_3PO_4 having pH equals to 1.5 and 1 *M* KOH electrolyte solutions. Voltages were transformed form SCE to reversible hydrogen electrode (RHE) by using the equation $E_{RHE} = E_{SCE} + 0.059\times pH + 0.241$, where E_{RHE} is the potential in terms of RHE and E_{SCE} is the potential in terms of SCE. CV curves were recorded to measure ECSA in the potential window 1 to 1.15 V vs RHE at different scan rates. The polarization curves were recorded by LSV at 1 mV/s scan rate in the potential window 1.05 to 1.75 V vs RHE (for OER) and 0.33 to −0.85 V vs RHE (for HER). The Tafel plots were obtained by the equation $\eta = a + b \times \log|j|$, where, *a* is intercept, *b* is the slope and *j* is current density. The electrochemical impedance spectroscopy (EIS) was studied by applying 10 mV AC amplitude in 0.1 MHz to 100 mHz frequency range. Long term catalytic stability studies were accomplished by chronoamperometry (CA) test at overpotentials. Further, overpotential (V) values were calculated for OER by subtracting the thermodynamic potential for OER (1.23 V) from the observed potential in terms of RHE. Using two electrode system, full cell elecrolyzer was made where deposited material electrodes were used as both an anode and cathode. The electrochemical behavior of the cell was studied by polarization curve and impedance measurements before and after long term overall water splitting performed by chronoamperometry in alkaline bath using PARSTAT 3000A-DX (AMETEK Scientific Instruments USA).

3. Results and discussion

3.1. Reaction mechanism

Growth mechanism for film formation is mainly divided into two types. In ion-by-ion mechanism, growth of materials takes place by deposition of ions on the substrate surface at the nucleation sites. On the other hand, in cluster-by-cluster mechanism, adsorption of colloidal particles leads to formation of nuclei and aggregation and coalescence facilitates the growth of thin film [29]. Synthesis of cobalt-iron phosphate was accomplished using superficial hydrothermal method on SS-substrates. Fundamentally, the stages of solution reaction are the nucleation, coalescence and growth of particle from liquid to solid phase formation which is nothing but the bottom-up approach. There are two classes of particle development such as heterogeneous and homogeneous nucleation followed by successive crystal growth. In homogeneous growth, the particle seeds formed within the solution and produced the precipitation of material. On the other hand, in heterogeneous growth, the nucleation of particle seeds formed at the substrate surface and consequently development of uniform material is possible.

Cobalt-iron phosphate synthesized by hydrothermal method with the variation of concentration ratio of cobalt and iron. The hydrolyzing agent used for the reaction is urea ($CO(NH_2)_2$) along with the precursors cobalt (II) chloride ($CoCl_2{\cdot}6H_2O$), iron (II) chloride ($FeCl_2$), and potassium dihydrogen orthophosphate (KH_2PO_4). At optimized reaction temperature (130 °C), water dissolved urea gets decomposed into ammonium hydroxide (NH_4OH) with the release of carbon dioxide (CO_2). Following reaction gives decomposition of water dissolved urea:

$$CO(NH_2)_2 + 3H_2O \rightarrow 2NH_4OH + CO_2 \uparrow \quad (1)$$

The formation of ammonium hydroxide in the reaction bath increases the pH of the solution to alkaline which further complexes the metal ions as:

$$CoCl_2.6H_2O + FeCl_2 + 2NH_4OH \rightarrow [Co(NH_3)]^{2+} + [Fe(NH_3)]^{2+} + 8H_2O + [4Cl^-] \quad (2)$$

Simultaneously, KH_2PO_4 gets decomposed into the dihydrogen phosphate ion as:

$$KH_2PO_4 \rightarrow \left[K^+\right] + \left[H_2PO_4^-\right] \quad (3)$$

The amine cations of cobalt $[Co(NH_3)]^{2-}$ and iron $[Fe(NH_3)]^{2-}$ get reacted with the phosphate anions $[H_2PO_4^-]$ and starts the nucleation of cobalt iron phosphate.

$$x[Co(NH_3)]^{2+} + (3-x)[Fe(NH_3)]^{2+} + 2\left[H_2PO_4^-\right] \rightarrow Co_xFe_{3-x}(PO_4)_2 + 3NH_3 \uparrow + 2H_2 \uparrow \quad (4)$$

The growth of cobalt-iron phosphate at the molecular stage take place with heterogeneous nucleation on the surface of SS-substrate. The superior and even thin layer of cobalt-iron phosphate forms by the growth of nuclides through coalescence. At 130 °C reaction time, the SS substrates get covered with uniform coating of material within the optimized reaction time.

3.2. Structural, morphological and elemental analysis

The structural properties of cobalt-iron phosphate at different compositional ratio, cobalt phosphate, and iron phosphate synthesized on SS-substrate which were examined by XRD analysis and

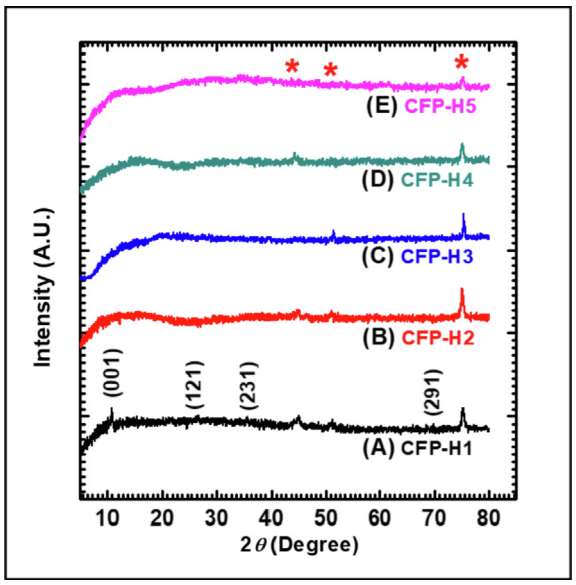

Fig. 1. Structural information of the cobalt iron phosphate catalysts: XRD patterns of hydrothermally synthesized cobalt iron phosphate thin films on SS substrates.

presented in Fig. 1. It is observed that, the cobalt phosphate (CFP-H1) show crystalline nature. The diffraction peaks at 2θ = 10.8°, 13.26°, 26.7°, 35.6°, and 69.8° can be indexed to (001), (020), (121), (231), and (291) planes, respectively corresponding to $Co_3(PO_4)_2{\cdot}4H_2O$ (JCPDS card no. 34-0844). The similar crystalline nature was reported earlier for cobalt phosphate by Katkar et al. [30]. The peaks marked with '*' are the diffraction peaks of SS substrate. As the small amount of iron was introduced (CFP-H2), the diffraction peaks of $Co_3(PO_4)_2{\cdot}4H_2O$ disappeared. The all other cobalt-iron phosphate at different compositional ratio, and iron phosphate materials are showing amorphous nature. The amorphous materials may give the large surface area and high electrocatalytic active sites which are favorable for water molecule adsorption and decomposition into O_2 and H_2.

Fig. 2 gives the Fourier transform infra-red spectra of the prepared materials which reveals the intermolecular bonding and

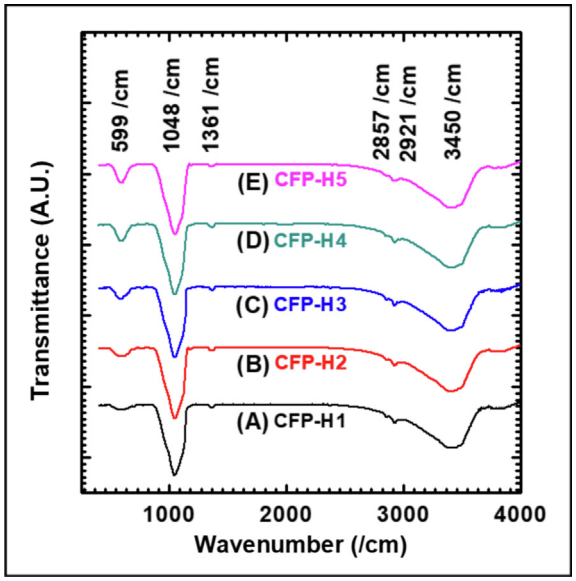

Fig. 2. Intermolecular bonding information of the cobalt iron phosphate catalysts: FTIR patterns of hydrothermally synthesized cobalt iron phosphate thin films on SS substrates.

their vibrational modes. Absorption peak at 599 /cm reveals the asymmetric bending vibrations of PO_4 bonding. It is observed that, as iron content increases absorption of the peak goes on increasing. The increase in peak intensity may be due to the coordination interaction between iron and phosphate molecules. The asymmetric stretching vibrations are observed by the sharp absorption at 1048 /cm [31]. Very small absorption band at 1361 /cm is assigned to the vibration of the CO_2 molecules raised from urea [32]. The hydrogen bonding in the interlayer is observed by the pair of small absorption peaks at 2857 /cm and 2921 /cm. Broad range at higher wavenumber around 3450 /cm is attributed to the stretching vibrations of the O—H molecules from the structural water. The FTIR result revealed that, there are phosphate and hydrous content present in the synthesized cobalt iron phosphate materials.

Material surface area, pore structure and pore size distribution of the cobalt phosphate (CFP-H1), cobalt iron phosphate (CFP-H3) and iron phosphate (CFP-H5) samples were studied by the N_2 adsorption/desorption isotherm and Barrett–Joyner–Halenda (BJH) method. The adsorption–desorption isotherms of the samples as shown in Figure S1(A) belongs to BET and isotherm of type-IV shape representing the mesoporosity and large adsorption energy [33]. With the 8.93 m^2/g, 11.86 m^2/g, and 4.45 m^2/g specific surface area of CFP-H1, CFP-H3 and CFP-H5, respectively, sample CFP-H3 shows highest specific surface area. This result underscores the usefulness of addition of iron into the cobalt in the escalating the surface area of the material. The lower surface area for CFP-H1 and CFP-H5 samples can be attributed to the observed dependence of surface area on the uneven overgrowth of crystals into a particle size distribution which is further observed in the FESEM images, and final Ostwald ripening which tends to the blocking of pores. The pore size distribution curves of the materials are calculated from Barrett–Joyner–Halenda (BJH) method shown in Figure S1 (B). Figure illustrates the pore sizes of the samples range from 5 to 15 nm, confirming the mesoporous structure of the synthesized materials and the average pore sizes are 10.64 nm, 6.12 nm, and 10.65 nm corresponding to CFP-H1, CFP-H3, and CFP-H5. The large specific surface area and small pore size can improve the electrolyte–electrode interface area, and huge number of electroactive positions for the –OH species adsorption and mass transfer, which may lead to enhanced electrochemical properties of the material.

For the analysis of valance electronic states existing in the elements of the synthesized material, XPS measurement was conducted. XPS spectra of CFP-H3 are presented in Fig. 3. In the survey scan spectrum, the occurrence of phosphorus, oxygen, iron and cobalt elements are observed as presented in the Fig. 3(A). The spectrum of Co2p given in Fig. 3(B) depicts the existence of prominent peaks as $Co2p_{3/2}$ at 781.66 eV and $Co2p_{1/2}$ at 797.29 eV and the alongside satellite peaks at 785.57 and 802.80 eV, correspondingly. It is confirmed from peaks position that the detected Co element has Co^{2+} electronic state [34,35]. Also for the Fe element, the main peak $Fe2p_{3/2}$ positioned at 710.93 eV and $Fe2p_{1/2}$ positioned at 724.45 eV (Fig. 3(C)) and have composed by two distinct peaks at 710.48 and 712.58 eV. Also, the peaks at 724.13 and 725.67 eV conforming Fe^{3+} and Fe^{2+} states in prepared sample. As shown in Fig. 3(D), the high resolution part of P element, P2p is composed of two diverse peaks, $P2p_{3/2}$ at 132.93 eV and $P2p_{1/2}$ at134.08 eV which are accredited to the metal phosphate (P—O—M) bond and phosphate group (P—O) related to P^{5+} oxidation state in phosphate series [36,37]. The O1s main peak is composed of three distinct peaks located at 529.58, 530.98 and 531.78 eV as shown in Fig. 3(E). The deconvoluted peaks (529.58 and 530.98 eV) denote the M–O and P—O bonding in metal, oxygen and phosphorus and the peak at 531.78 eV corresponds to surface adsorbed water molecules [38].

Topographical change with the composition variation of cobalt and iron is observed by FESEM and shown in Fig. 4. Images at dif-

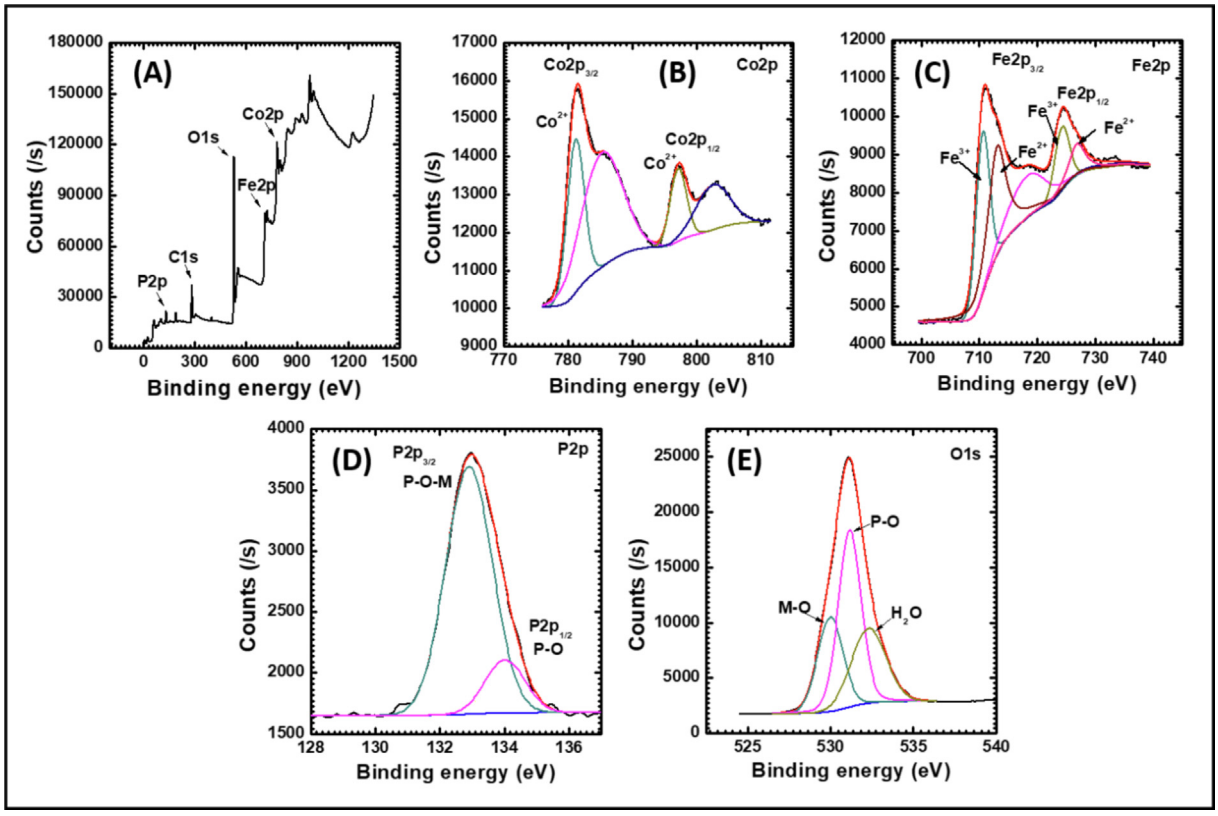

Fig. 3. Electronic state determination of the cobalt iron phosphate catalysts: XPS spectra of sample CFP-H3 **(A)** survey spectrum, high resolution spectrum of **(B)** Co2p, **(C)** Fe2p, **(D)** P2p, and **(E)** O1s.

ferent magnifications (1kX, 10 kX, 20 kX) showed that, as the composition varies from CFP-H1 to CFP-H5, the morphology varies from microchips (CFP-H1) (Fig. 4(A-C)) to micrometric cubes and pyramids (CFP-H5) (Fig. 4(M−O) followed by submicrometric strips having nanometric thickness (CFP-H3) (Fig. 4(G-I)). As iron introduced (CFP-H2), microchips get turned into microplates with thickness ~300 nm and length ~1.5 μm (Fig. 4(D-F)). As further increase in iron to equal contribution of cobalt (CFP-H3), thickness of the microplates reduced to ~45 nm, width becomes ~380 nm and length becomes ~0.8 μm. For the sample CFP-H4, iron concentration exceeds and surface starts to convert into large and agglomerated grains (Fig. 4(J-L)). Whole area covered with grains having size ~3 to 4 μm and some agglomerated large particles with size ~9 μm. For sample CFP-H5, it is observed that, large particles (~10 to 20 μm) made from the agglomeration of submicrometric pyramids distributed over the surface. The corresponding microstructures are formed by the aggregation of amorphous nanoparticles, and similar amorphous microstructures have reported previously [39,40].

Morphological observations revealed that, cobalt phosphate (CFP-H1) and iron phosphate (CFP-H5) materials have large particle size and smaller surface area. These observations are associated with N_2 adsorption/desorption isotherm (BET analysis). On the other hand, cobalt-iron phosphate (CFP-H3) material have smaller microplates with nanometer thickness reveals enormous surface area and hence huge number of electrochemical active sites for water molecule adsorption and oxidation which is advantageous to water splitting application. The rate of reaction influenced by the composition of cobalt and iron caused the morphological evolution from microchips to microplates and microstrips and further pyramids [41].

Chemical compositional analysis was made with the help of EDS analysis associated with FESEM. The elemental mapping is plotted in Figure S2(A-E). The EDS spectra evidenced that, the hydrous cobalt-iron phosphate consisted of cobalt, iron, phosphorus, and oxygen elements without any other impurity. The atomic percentage ratios of cobalt to iron are 100:0, 74.62:25.38, 48.24:51.76, 22.99:77.01, and 0:100 for CFP-H1, CFP-H2, CFP-H3, CFP-H4, and CFP-H5, respectively. Also, it is observed that, approximately constant phosphorous and oxygen atomic percentage is found in all samples, only difference is observed in the cobalt and iron atomic ratio and it is quite similar to experimental ratio. As shown in Table S1, as per the synthesis ratio, the atomic percentage of cobalt in the prepared material decreases and atomic percentage of iron increases. Atomic percentages of P and O are tabulated, which reveals that, in all samples P and O are in 1:4 proportion which confirms the formation of phosphate (PO_4^{3-}) rather than pyrophosphate ($P_2O_7^{4-}$) and triphosphate ($P_3O_{10}^{5-}$). The observed atomic ratios are very close to the experimental molar ratios of the materials. From the EDS analysis, it is confirmed that synthesized materials are cobalt iron phosphate at different molar ratio of cobalt and iron, and it is responsible for morphological evolution.

3.3. Electrochemical catalytic performance analysis

The electrochemical catalytic performance of the materials may influence by the composition of metals (cobalt and iron), therefore we optimized the atomic percentage of cobalt and iron to choose the best catalyst. In order to confirm the hypothesis, the electrocatalytic oxygen and hydrogen evaluation activities were investigated in terms of OER, HER and overall water splitting. The cobalt phosphate, cobalt-iron phosphate and iron phosphate materials were electrochemically examined to split water in the forms of OER and HER in basic and acidic electrolytes, correspondingly. The best performing sample was further characterized for overall water

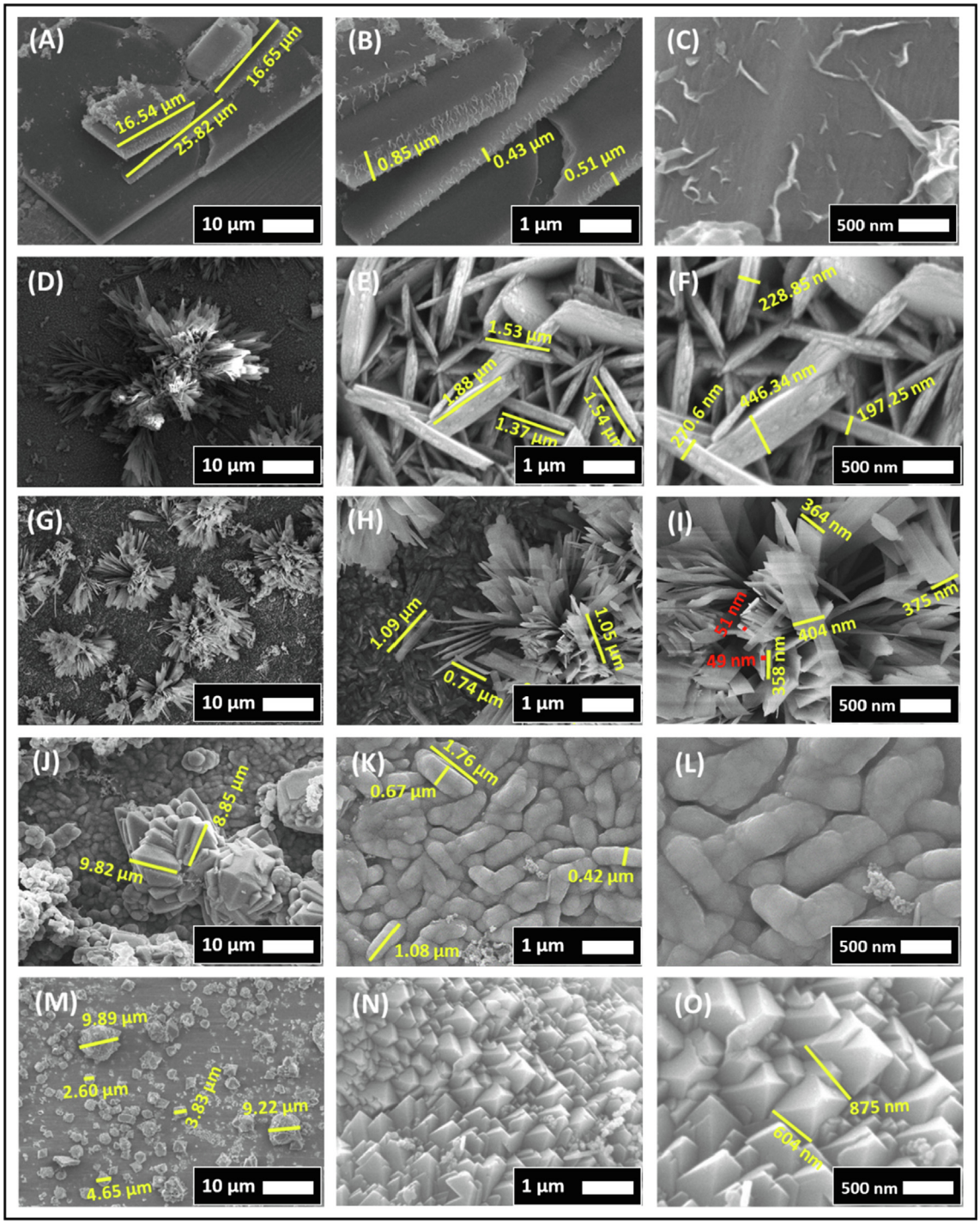

Fig. 4. Surface morphological study of the cobalt iron phosphate catalysts: FESEM images at different magnifications of **(A-C)** CFP-H1, **(D-F)** CFP-H2, **(G-I)** CFP-H3, **(J-L)** CFP-H4, and **(M–O)** CFP-H5.

splitting and long duration stability by making full cell electrolyzer for their commercial application.

Before going to study electrocatalysis in terms of OER and HER, it is important to measure electrochemically active surface area (ECSA) of the prepared materials. ECSA is directly related to the double layer capacitance (C_{dl}) of the material. To measure C_{dl}, cyclic voltammograms were recorded for each electrode in the small potential range with the open circuit potential (OCP) is at the middle of that window, where Faradic reactions not occurred. Fig. 5(A-E) shows the CV curves of the electrodes recorded at different scan rates. C_{dl} is calculated by plotting the anodic charging currents (i_c) at OCP of each CV curve against the scan rate by the equation:

$$i_c = \upsilon C_{dl} \tag{5}$$

Where, υ is the scan rate. It yields a straight line with slope equals to C_{dl} as shown in Fig. 5(F). The plot reveals the values of C_{dl} are 0.42, 1.93, 3.31, 2.52, and 0.28 mF for CFP-H1, CFP-H2, CFP-H3, CFP-H4, and CFP-H5 thin film electrodes, respectively. The ECSA were further calculated by the equation:

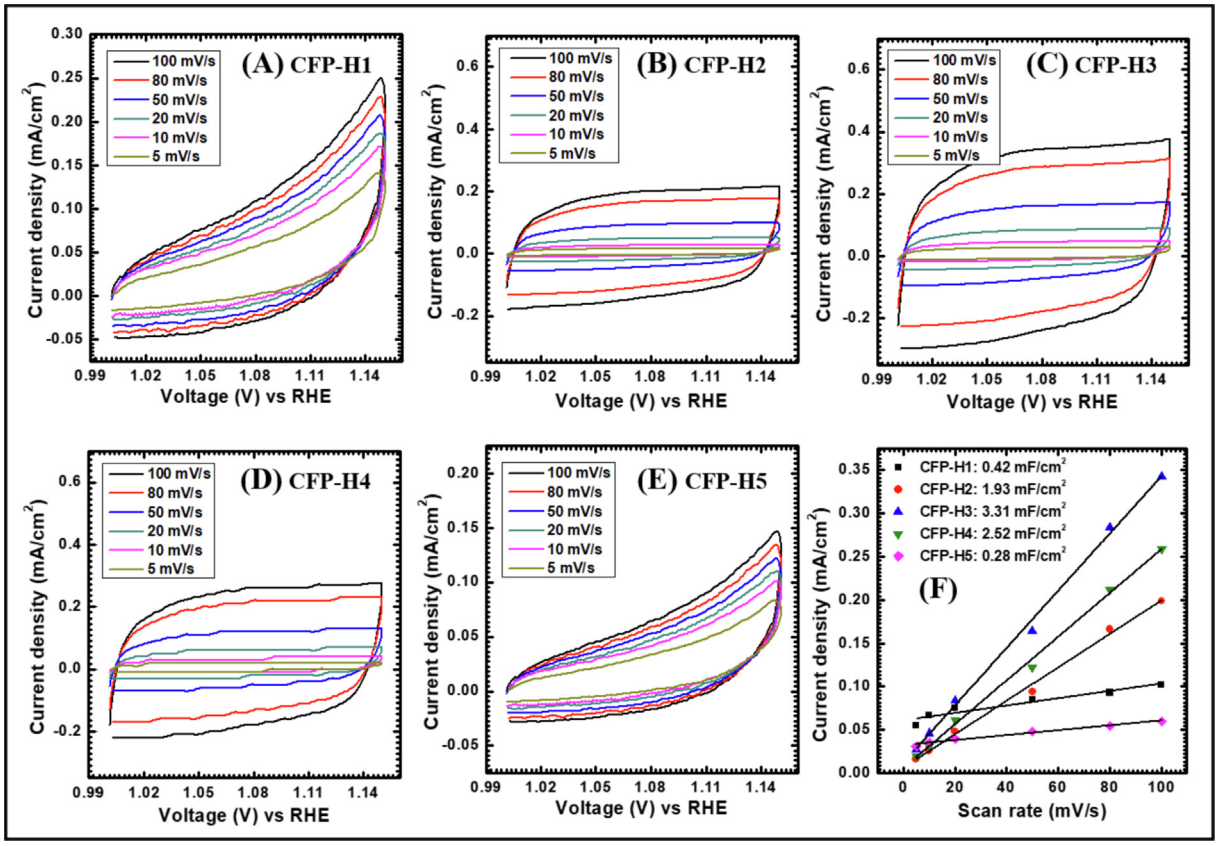

Fig. 5. Electrochemical active surface area (ECSA) analysis of the cobalt iron phosphate catalysts: The CV curves of **(A)** CFP-H1, **(B)** CFP-H2, **(C)** CFP-H3, **(D)** CFP-H4, and **(E)** CFP-H 5 at various scan rates in a small potential range (1.00–1.15 V vs. RHE), and **(F)** their anodic current linear fit for C_{dl} values.

$$\text{ECSA} = C_{dl}/C_s \quad (6)$$

Where, C_s is the general specific capacitance of an atomically smooth planar surface of the material per unit area under identical electrolyte conditions. Typically, general specific capacitance C_s in alkaline solution is 0.04 mF [42]. The highest ECSA calculated is 82.75 cm^2 for CFP-H3 electrode. In contrast, other electrodes show quite fare values such as 10.55, 48.25, 63, and 7.05 cm^2 for CFP-H1, CFP-H2, CFP-H4, and CFP-H5 electrodes, respectively. Also, the roughness factor (RF) is an index which gives the electrocatalytic interface texture and can be calculated by dividing the ECSA with the geometric area of the electrode in contact with electrolyte. In this study, we use 1 cm^2 area of the film to measure electrochemical activities. Hence the RF values are 10.55, 48.25, 82.75, 63, and 7.05 for CFP-H1, CFP-H2, CFP-H3, CFP-H4, and CFP-H5 electrodes, respectively. The relatively large RF indicates the high electrocatalytic sites for exposing with electrolyte and favorable diffusion kinetics for the reactants. The electrode CFP-H3 demonstrate very high ECSA and RF than the other electrodes are consistent with the BET surface analysis.

To study OER activity of the prepared material electrodes, the linear sweep voltammograms (LSV) were recorded at 1 mV/s scan rate in the potential range 1.05 to 1.75 V vs. RHE as shown in Fig. 6 (A). The nature of the all LSV polarization curves is similar and continuous increase in current density with change in cobalt to iron ratio from 100:0 to 50:50. By the LSV curves, it is confirmed that most electrochemically active material composition is 50:50 (sample CFP-H3). Sample CFP-H3 requires exponentially lowest overpotential of 251.9 mV to deliver 10 mA/cm^2 current density suggesting outstanding oxygen evoluting catalyst. In contrast, other materials CFP-H1 (300.8 mV), CFP-H2 (298.9 mV), CFP-H4 (295.1 mV) and CFP-H5 (298.9 mV) exhibited considerably high overpotentials to reach the current density of 10 mA/cm^2 as comparatively shown by bar diagram in Fig. 6(B).

When the catalyst has higher OH^- ion attraction to adsorb at the surface and to form an intermediate, O_2 molecule formation at the catalyst surface becomes easier. If those intermediate states formation is faster, then the reaction steps are rate determining. The reaction rate kinetics for OER was determined by the Tafel slope, which can be obtained by plotting applied potential against the logarithmic current density at the shoot-point of current density. The Tafel plot is shown in Fig. 6(C) which reveals the Tafel slope is 39.3 mV/dec for the electrode CFP-H3, is lower than 45.7 mV/dec (CFP-H1), 43.9 mV/dec (CFP-H2), 41.5 mV/dec (CFP-H4), and 44.7 mV/dec (CFP-H5). It indicates that, highly efficient reaction kinetics at CFP-H3 electrode surface and the OER reaction process is faster. The EIS plot has shown that there is much smaller charge transfer resistance (R_{ct}) to CFP-H3 electrode (Fig. 6(D)). The fitted R_{ct} values are 0.58, 0.342, 0.088, 0.671, and 0.663 Ω for CFP-H1, CFP-H2, CFP-H3, CFP-H4, and CFP-H5 electrodes, respectively. It reveals that, easy charge transfer process is one of the reason for low overpotential.

Catalytic stability is crucial criteria to evaluate the electrode material for long term usage as OER or HER catalyst. The chronoamperometric test at constant overpotential to achieve 10 mA/cm^2 current density was further studied for 24 h. The stability test plot is shown in Fig. 7(A) which reveals that, initially material activated continuously hence, current density becomes almost double and for the further time period, material delivers constant current up to 24 h. It is observed that, during the catalysis, material become catalytically more active and shows enhanced performance. It may be due to the involvement of Co^{2+}, Co^{3+} and likely Co^{4+}, and similarly Fe^{2+}, and Fe^{3+} oxidation states in the redox

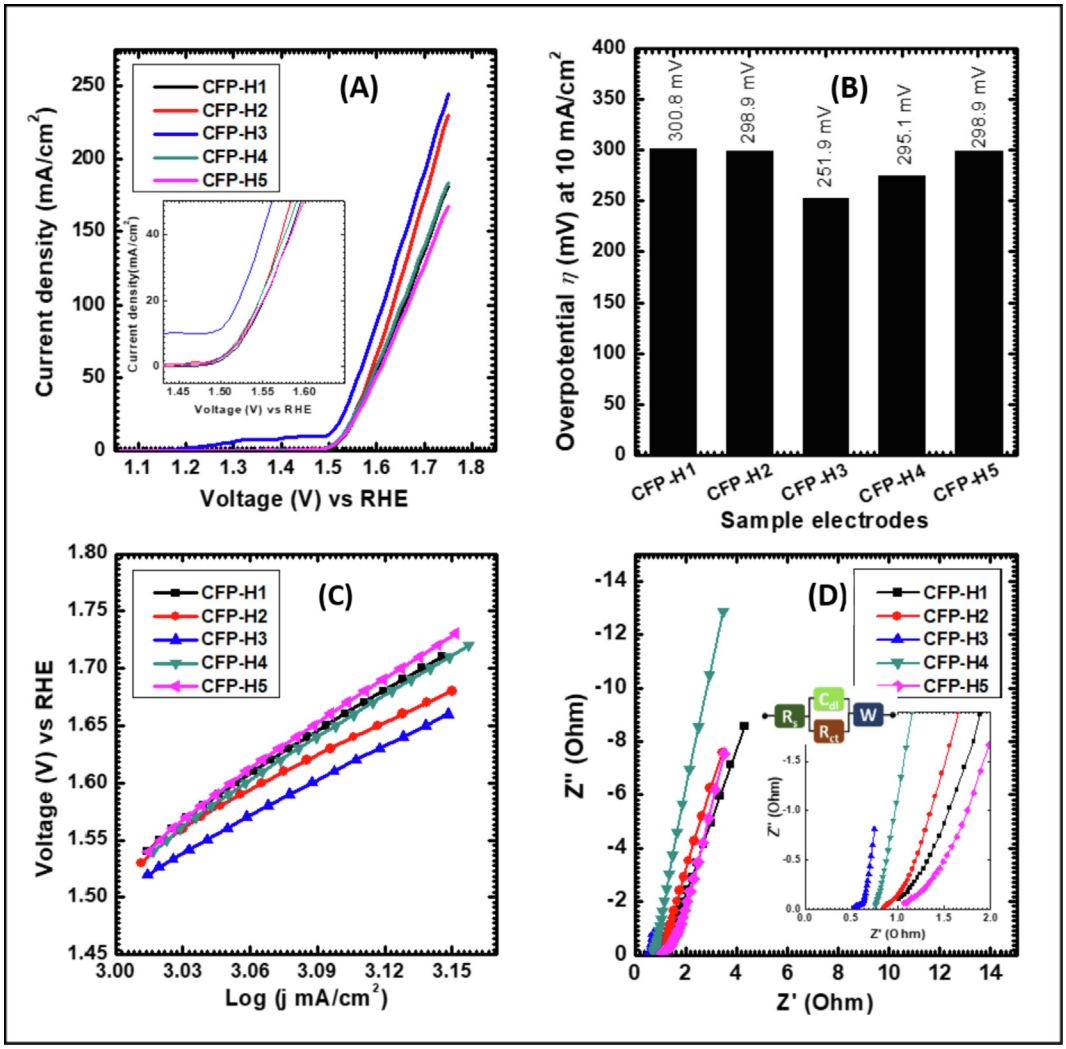

Fig. 6. Electrochemical OER analysis of the cobalt iron phosphate catalysts: (A) LSV polarization curves recorded with scan rate 1 mV/s, inset shows magnified view at current shoot point, **(B)** bar diagram of overpotentials observed at 10 mA/cm^2 current density, **(C)** Tafel plots derived from LSV curves, **(D)** EIS recorded at OCP, inset figures gives the magnified image of EIS at higher frequency region and fitted equivalent circuit.

cycles of active centers [43]. From the stability test, it is concluded that, the CFP-H3 is favorable for long duration catalysis with enhanced performance. The comparative LSV plot before and after 24 h catalysis is shown in Fig. 7(B), which discloses that overpotential decreases from 251.9 to 250 mV and current density increases rapidly when applying higher potential. Inset figure shows the change in Tafel slope from 39.3 to 35.2 mV/dec after catalytic stability. The EIS was performed after stability test and it is observed that, the R_{ct} decreases from 0.088 Ω to 0.037 Ω (Fig. 7(C)). The fitted EIS parameters are tabulated in Table S2.

Another half reaction of water splitting is nothing but the hydrogen evolution reaction (HER). Theoretically HER require 0 V potential vs RHE, although it is more favorable in acidic media. The polarization curves were recorded in the potential range 0.32 to −0.85 V vs RHE as shown in Fig. 8(A). All LSV curves show identical nature, rapid and steeper current increase with increase in potential. The overpotentials measured at 10 mA/cm^2 current density for all electrodes as 282.57, 202.93, 55.50, 152.25, and 368.01 mV for CFP-H1, CFP-H2, CFP-H3, CFP-H4, and CFP-H5 electrodes, respectively. This revealed that, CFP-H3 electrode requires lowest overpotential to deliver 10 mA/cm^2 current density. The trend of overpotential is shown in Fig. 8(B) by bar diagram. The rate determining kinetics was studied by plotting Tafel slope to evaluate faster hydrogen evolution reaction. Fig. 8(C) gives the Tafel plot determined from LSV curves for all sample electrodes, which depicts lower Tafel slope for the same material which have low overpotential. The Tafel slope for CFP-H1, CFP-H2, CFP-H3, CFP-H4, and CFP-H5 electrodes are 94.78, 90.15, 73.64, 85.25, and 91.72 mV/dec, respectively. The charge transfer becomes easier (3.63 Ω) for CFP-H3 electrode, measured by EIS measurement for each electrode (Fig. 8(D)). The fitted R_{ct} values are 13.14, 6.52, 3.63, 9.54, and 11.09 Ω for CFP-H1, CFP-H2, CFP-H3, CFP-H4, and CFP-H5 electrodes, respectively. Further, the HER catalytic stability test was performed by chronoamperometry at overpotential for 24 h. By the test, it is observed that, material become highly active continuously and shows enhanced current density throughout the time (Fig. 9(A)). The performance is compared by LSV curves measured before and after the HER catalysis. The decrease in overpotential after 24 h catalysis from 55.5 to 37.3 mV is observed due to the continuous activation of the catalytic sites (Fig. 9(B)). Inset of Fig. 9(B) give the comparative plot of Tafel slope, and it appears to be 68.97 mV/dec after 24 h catalysis. Fitted EIS curves before and after stability test shows that the C_{dl} decreased from 3.63 to 1.87 Ω after 24 h catalysis due to the enhanced active sites (Fig. 9(C)). The fitted EIS parameters are tabulated in Table S2. From the 24 h HER catalytic stability, it

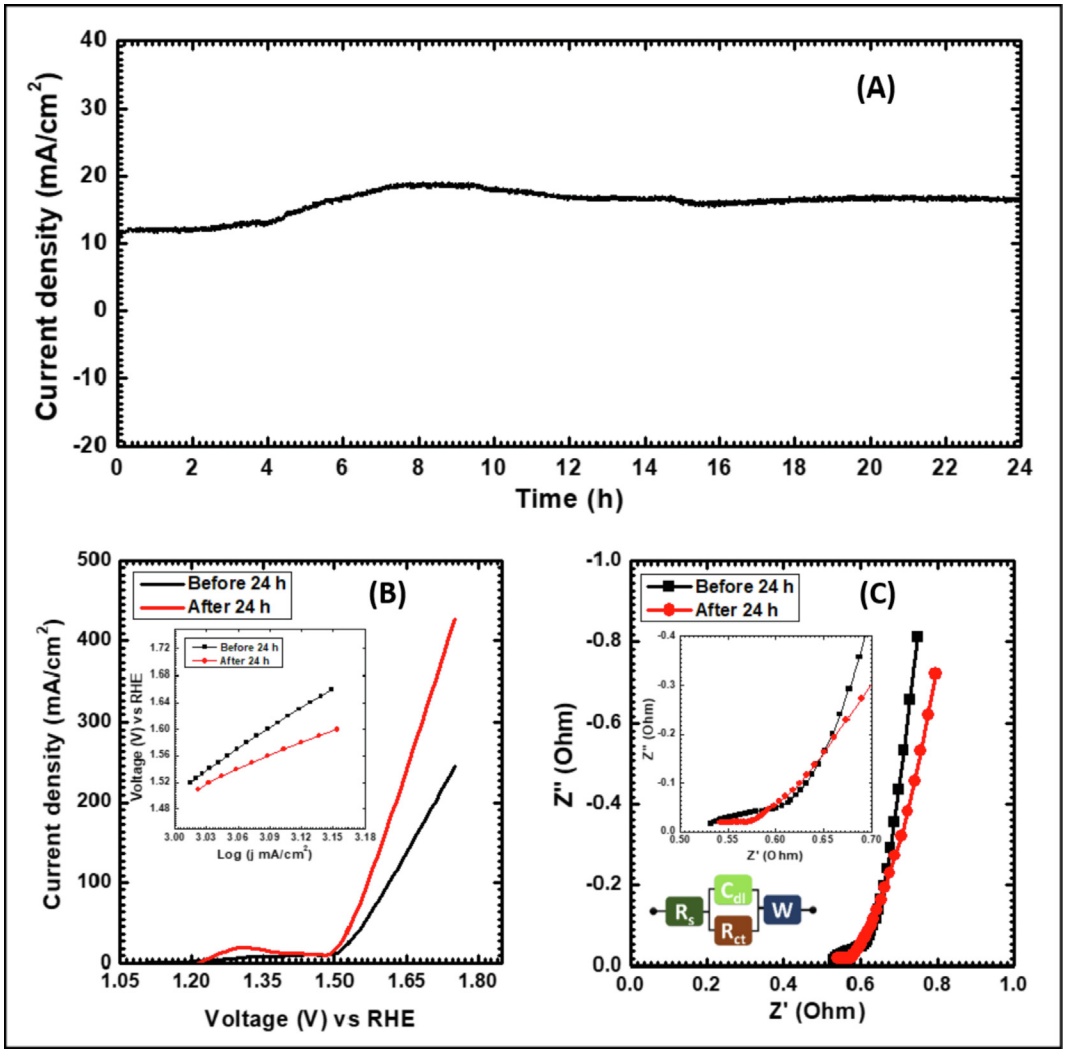

Fig. 7. Electrochemical OER stability of the cobalt iron phosphate catalyst: (A) CA (*I-t*) plot for electrocatalytic stability study, **(B)** comparative study of LSV before and after 24 h OER catalysis, inset figure gives the Tafel plots, and **(C)** EIS recorded at OCP before and after 24 h catalysis, inset figures gives the magnified image of EIS at higher frequency region and fitted equivalent circuit.

is concluded that, the material does not show stable current density, with time the current goes on increasing and hence the performance is also increasing. From the HER continuous 24 h catalysis and analysis after the catalysis, it is concluded that, the continuous increase in electrochemical performance with decrease in overpotential for the CFP-H3 catalyst.

The full cell electrochemical water splitting analysis and catalyst characteristics after long duration catalysis are very much important to insist the synthesized catalysts to be commercially feasible. For the purpose, HER of the CFP-H3 electrode was further carried in 1 M KOH electrolyte. The LSV curve and Tafel plot are shown in Figure S3 (supporting information). The measured overpotential is 126.4 mV at 10 mA/cm^2 current density and Tafel slope of 107.3 mV/dec. The long term catalytic property of the material was studied for overall water splitting in same alkaline bath by constructing a full cell device using the cobalt iron phosphate thin films as anode and cathode. The CA test for 100 h continuous water splitting was performed at an overpotential to deliver 10 mA/cm^2 current density in alkaline medium (1 M KOH). The CA *I-t* plot is shown in Fig. 10(A). It is observed that, there is continuous small increment in current density with time due to the activation of the material and then a small reduction in current every day because of the dehydration of the electrolyte. After adjusting the level by the addition of electrolyte, increment in the current also observed. The LSV curves before and after catalytic stability test were recorded in the potential window 0 to 2 V at scan rate of 1 mV/s and are shown in Fig. 10(B). It revealed that, there is decrease in the potential from 1.78 V to 1.75 V to deliver 10 mA/cm^2 current density. The decrement in overpotential may attributed to the material activation. The EIS was measured initially and after 100 h at OCP and very small decrease in the charge transfer resistance is observed after the catalysis as shown in Fig. 10(C). After demonstrating the enhanced catalytic performance for 100 h stability test, it proves their strongest candidature for forthcoming alkaline electrolysis. The evaluation of electrochemical study before and after 100 h catalysis is given in Table S3. As a benchmark, the overpotentials for OER and HER at 10 mA/cm^2 current density, corresponding Tafel slopes and stability study were compared with the previously reported cobalt iron phosphate catalyst materials (Table S4), which confirms the outstanding performance of present investigation.

3.4. Postmortem analysis

The influences of long term electrochemical testing on the structural, electronic state and morphology were studied by con-

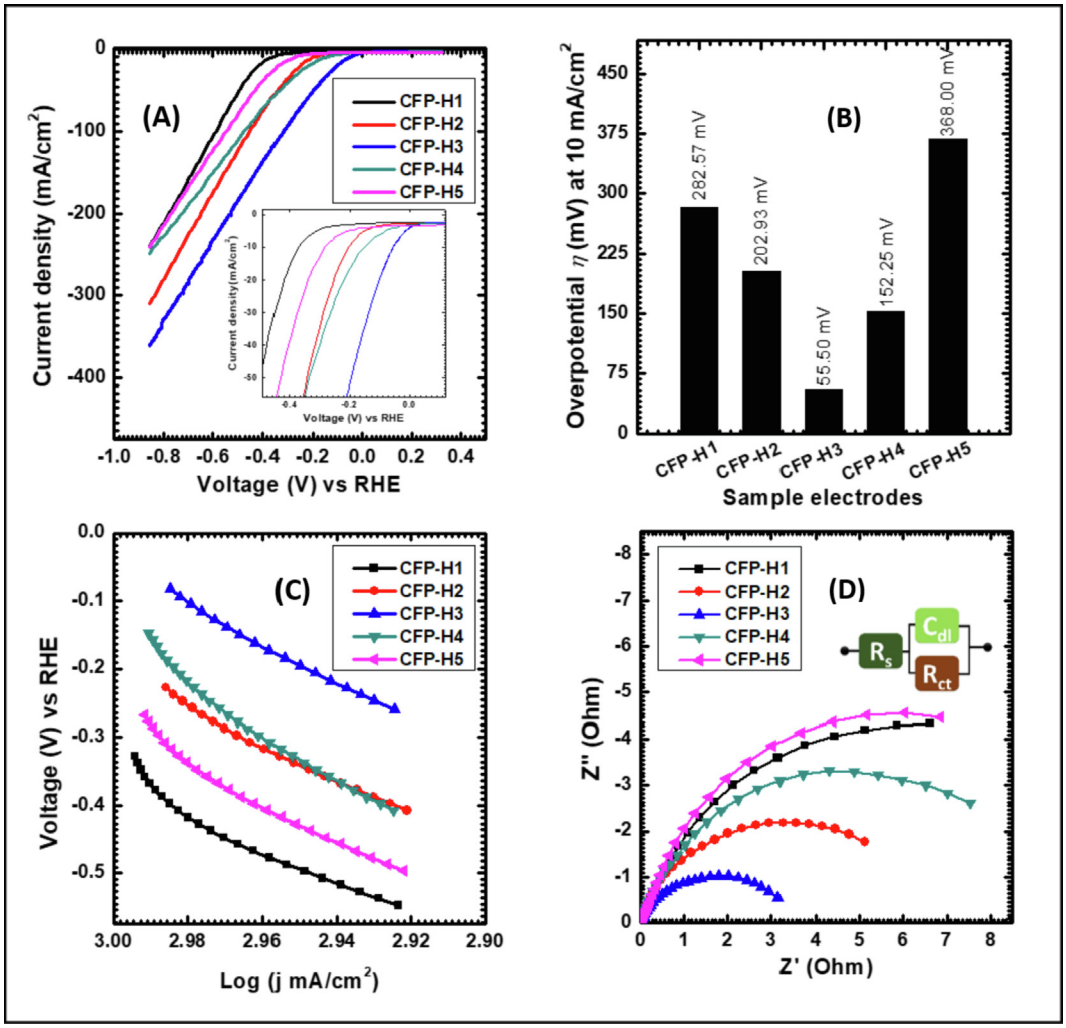

Fig. 8. Electrochemical HER analysis of the cobalt iron phosphate catalysts: (A) LSV polarization curves recorded with scan rate 1 mV/s, inset shows magnified view at current shoot point, **(B)** bar diagram of overpotentials observed at 10 mA/cm^2 current density, **(C)** Tafel plots derived from LSV curves, **(D)** EIS recorded at OCP and fitted equivalent circuit.

ducting the postmortem characterizations of the thin films restored from the electrochemical cell. The collected thin films were kept in double distilled water to washout the ions of electrolyte. XRD analysis was then performed and compared with the pattern of same material before long term electrolysis as shown in Figure S4. The peaks marked with star (*) are due to the diffraction from the crystal planes of SS substrate. There is no any diffraction peak observed in the sample after long term electrolysis. It reveals that the material remains amorphous in nature after electrochemical testing. The amorphous materials can provide large surface area and hence large number of active sites and easy ion transfer. Also, the surface morphology was analyzed by the FESEM. It is observed that, there is no observable change in the surface topography after the long term catalysis as shown in Figure S5 (A), and confirms the robustness of the material. The EDS analysis after catalysis gives the almost same stoichiometry with negligible loss of phosphorus as shown in Figure S5(B).

Further, for the examination of the electronic states present in the sample after electrochemical testing, x-ray photoelectron spectroscopy (XPS) measurements were carried out. The survey spectrum reveals the presence of P, C, O, Fe, and Co elements in the catalyst material as shown in Figure S6(A). Spectrum of Co2p at high resolution (Figure S6(B)), which reveals the presence of main peaks at 780.23 eV as $Co2p_{3/2}$ and at 795.33 eV as $Co2p_{1/2}$ and their corresponding satellite peaks at 785.98 eV and 802.48 eV, respectively. The peak $Co2p_{3/2}$ is composed with two peaks at 779.98 eV and 781.43 eV corresponding to Co^{3+} and Co^{2+} states, respectively. Also, the peak $Co2p_{1/2}$ is composed by two peaks at 795.03 eV and 796.33 eV corresponding to Co^{3+} and Co^{2+} states, respectively [34]. Similarly, Figure S6(C) shows the high resolution spectra of Fe2p states. It is observed that, the prominent peaks $Fe2p_{3/2}$ and $Fe2p_{1/2}$ located at 710.68 and 724.23 eV and two satellite peaks at 717.78 eV and 732.13 eV. It is observed that, the prominent peak $Fe2p_{3/2}$ is composed by the two peaks at binding energies 710.23 and 712.18 eV, and $Fe2p_{1/2}$ by the two peaks at binding energies 723.93 and 725.98 eV corresponding to Fe^{3+} and Fe^{2+} electronic states, respectively. The presence of both Fe^{2+} and Fe^{3+} electronic states of Fe atoms and Co^{2+} and Co^{3+} electronic states of Co atoms are observed due to the oxidation of the material and partial conversion from Fe^{2+} to Fe^{3+} and Co^{2+} to Co^{3+} during 100 h continuous electrolysis. Similarly, the peak of phosphorous is deconvoluted into the two peaks with $P2p_{3/2}$ at 132.33 eV attributed to the metal–oxygen-phosphorous (P—O—M), and $P2p_{1/2}$ at 133.13 eV known as phosphate group (P—O) bond in phosphate series corresponding to P^{5+} oxidation state (Figure S6(D)) [36]. Low peak intensity compared with the XPS before catalysis confirms that there is loss of phosphorous content with the partial transformation of phosphate into the stable metal oxides after 100 h catalysis. Also,

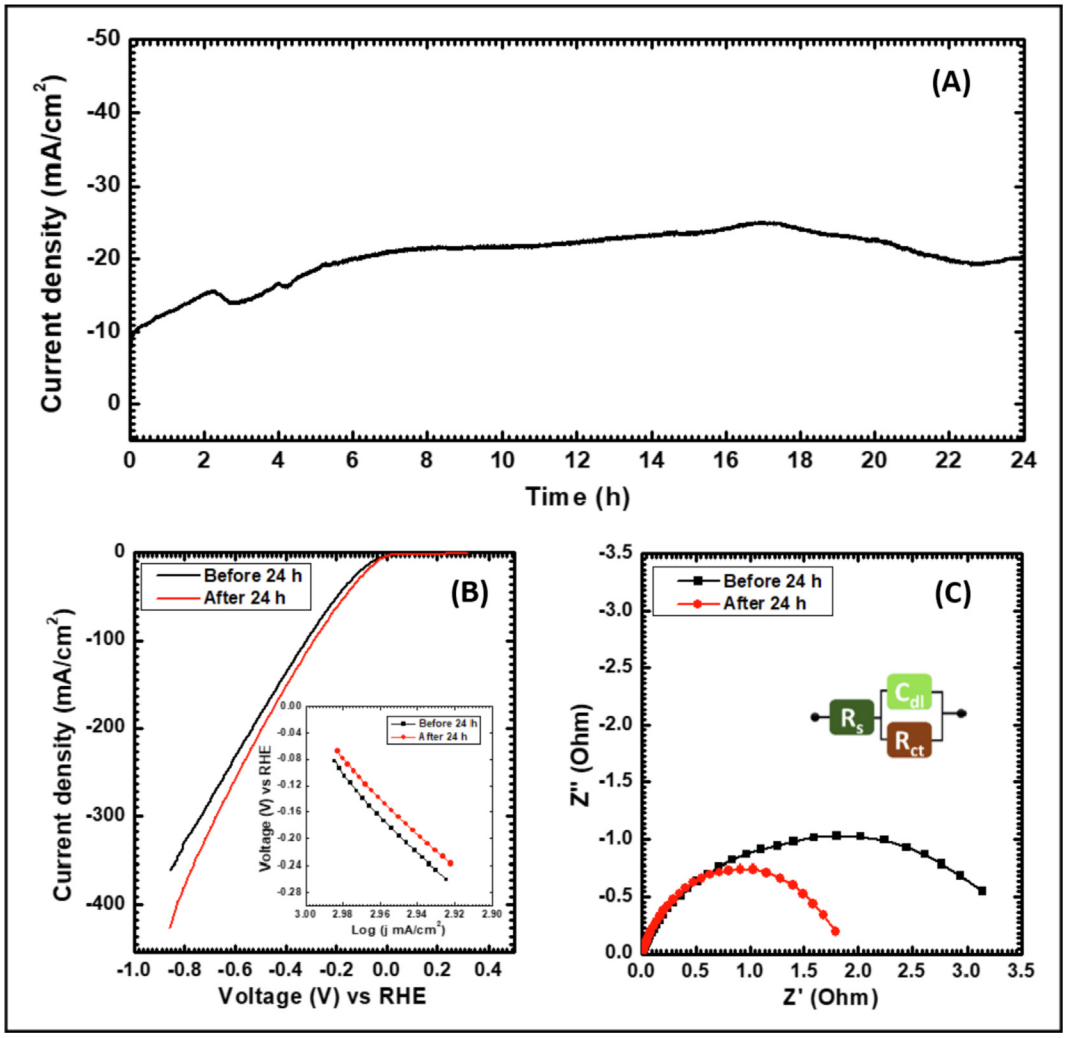

Fig. 9. Electrochemical HER stability of the cobalt iron phosphate catalyst: (A) CA (*I-t*) plot for electrocatalytic stability study, **(B)** comparative study of LSV before and after 24 h OER catalysis, inset figure gives the Tafel plots, and **(C)** EIS recorded at OCP before and after 24 h catalysis, inset figures gives an equivalent circuit.

the O1s main peak is composed of three distinct peaks located at 529.60, 530.76 and 531.61 eV as shown in Figure S6(E). The strong intense peak at 529.35 eV attributed to the metal–oxygen (M–O) bond [38]. Deconvoluted peak at 530.76 eV represent P—O bond in phosphate and 531.61 eV attributed to surface adsorbed water molecules. It is confirmed that, the electronic states attaining to the higher states of the metal atoms in the material are beneficial for the electrochemical catalysis process [43]. As compared to the XPS before catalysis, P—O bond intensity decreased and M–O bonding increased.

Summarizing, the hydrothermally synthesized binder free cobalt iron phosphate thin films gives the outstanding performances for electrochemical OER, HER and overall water splitting with the long term durability. The electrochemical performance is attributed to the unique composition of the metals and the phosphate ligands which facilitates the favorable conditions for electrolyte ion adsorption and oxidation. Also the amorphous and mesoporous nature of cobalt iron phosphate offers large number of electrochemical active sites and provides favorable conditions for material activation and hence enhancement in current density. Conversion of Co^{2+} to Co^{3+} and Fe^{2+} to Fe^{3+} states are beneficial for the enhancement in electrocatalytic performance [28]. Upon changing the composition of cobalt and iron, tuning the morphology helps to enhance the catalytic process. The synergistic effect of both metal atoms improves the electrical conductivity and metal-to-metal partial-charge-transfer process which result the high current density and small overpotentials.

4. Conclusions

The electrochemical water splitting in terms of OER, HER, and overall water splitting was demonstrated by using cobalt iron phosphate as an appropriate electrocatalyst. Binder free synthesis of amorphous cobalt iron phosphate thin films on stainless steel substrates were achieved by hydrothermal process. By changing the concentrations of cobalt and iron, the morphology varies from microchips (CFP-H1) to submicrometric strips having few nanometers thickness (CFP-H3) to micrometric cubes and pyramids (CFP-H5). Such a mesoporous submicrometric strips like cobalt iron phosphate required the smallest overpotential of 251.9 mV to deliver 10 mA/cm^2 current density in alkaline medium with the Tafel slope of 35.2 mV/dec for OER. Upon testing for HER in acidic medium for 24 h catalysis, only 37.3 mV overpotential is required for 10 mA/cm^2 current density. The long term (100 h) overall water splitting achieved by configuring two electrode system in same alkaline bath. Only 1.75 V potential is needed to split water molecule into the H_2 and O_2 after continuous water splitting. This work conclusively demonstrates the overall water splitting in minimum

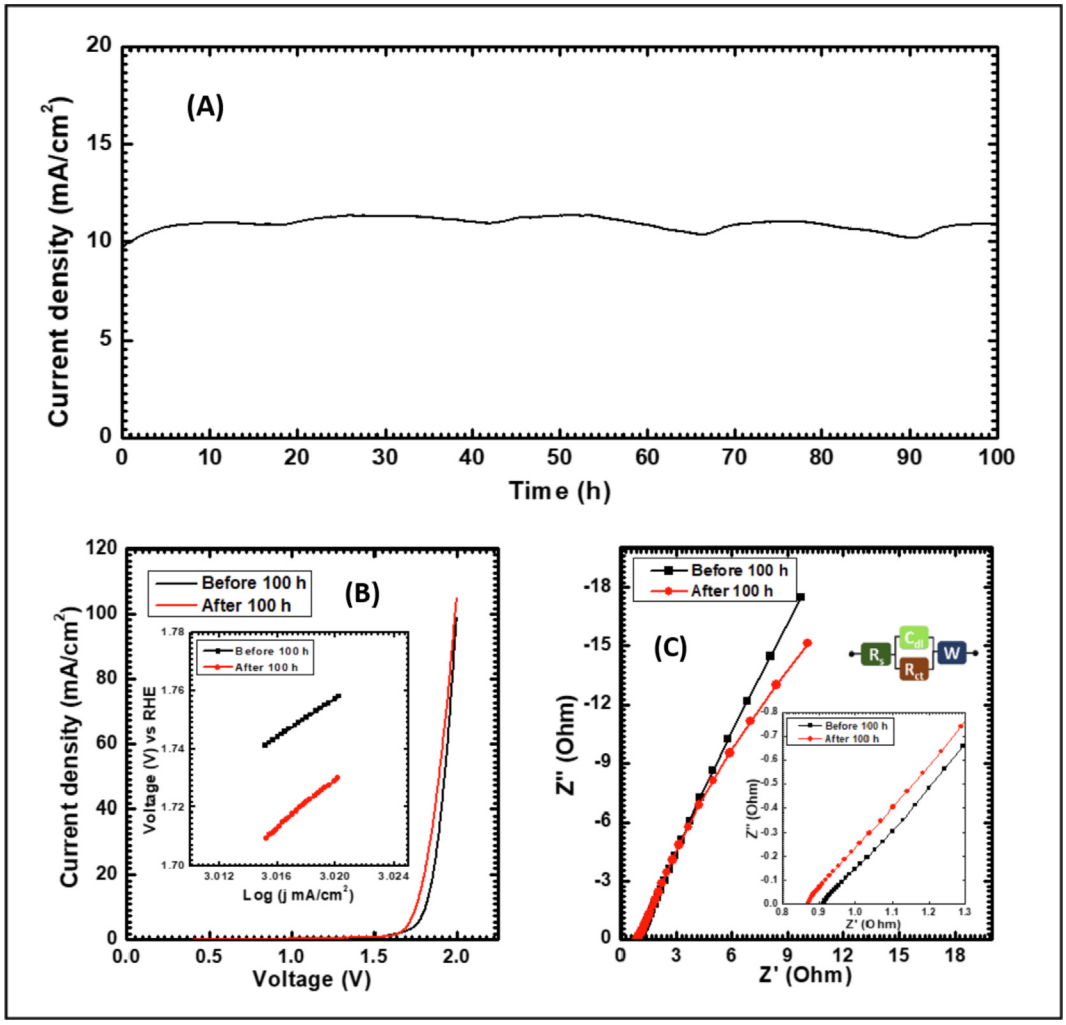

Fig. 10. Electrochemical overall water splitting stability of the cobalt iron phosphate catalyst: (A) CA (*I-t*) plot for electrocatalytic stability study in 1 *M* KOH electrolyte, **(B)** comparative study of LSV before and after 100 h catalysis, inset figure gives the Tafel plots, and **(C)** EIS recorded at OCP before and after 100 h catalysis, inset figure gives magnified EIS at higher frequency and the fitted equivalent circuit.

input energy by the cost effective, non-noble, and robust electrocatalyst which helps in future for the design of highly efficient electrolyzer and fuel cells for energy conversion.

CRediT authorship contribution statement

Suraj A. Khalate: Conceptualization, Methodology, Writing – original draft. **Sujit A. Kadam:** Resources. **Yuan-Ron Ma:** Resources. **Sachin B. Kulkarni:** Resources. **Vinayak G. Parale:** Resources. **Umakant M. Patil:** Supervision.

Declaration of Competing Interest

The authors declare that they have no known competing financial interests or personal relationships that could have appeared to influence the work reported in this paper.

Acknowledgment

The author Mr. Suraj A. Khalate acknowledges the Chhatrapati Shahu Maharaj Research Training and Human Development Institute (SARTHI), Pune (Government of Maharashtra) for awarding as SARTHI FELLOW and the financial support under the Chhatrapati Shahu Maharaj National Research Fellowship (CSMNRF-2019).

Appendix A. Supplementary data

Electronic supporting information contains data of EDS analysis, tables containing electrochemical analysis, electrochemical performance comparative study of present work with the previously reported cobalt iron phosphate materials, and postmortem characterizations like XRD, FESEM, EDS, and XPS. Supplementary data to this article can be found online at https://doi.org/10.1016/j.jcis.2022.01.015.

References

[1] H. Khatib, IEA world energy outlook 2011-A comment, Energy Policy 48 (2012) 737–743, https://doi.org/10.1016/j.enpol.2012.06.007.
[2] C. Cometto, A. Ugolotti, E. Grazietti, A. Moretto, G. Bottaro, L. Armelao, C. Di Valentin, L. Calvillo, G. Granozzi, Copper single-atoms embedded in 2D graphitic carbon nitride for the CO_2 reduction, npj 2D Mater. Appl. 5 (1) (2021), https://doi.org/10.1038/s41699-021-00243-y.
[3] J.F.d. Brito, G.G. Bessegato, J.A.L. Perini, L.D.d.M. Torquato, M.V.B. Zanoni, Advances in photoelectroreduction of CO_2 to hydrocarbons fuels: Contributions of functional materials, J. CO_2 Util. 55 (2022), https://doi.org/10.1016/j.jcou.2021.101810 101810.
[4] S.A. Khalate, R.S. Kate, R.J. Deokate, A review on energy economics and the recent research and development in energy and the Cu_2ZnSnS_4 (CZTS) solar cells: A focus towards efficiency, Sol. Energy 169 (2018) 616–633, https://doi.org/10.1016/j.solener.2018.05.036.

[5] Y. Shi, B. Zhang, Recent advances in transition metal phosphide nanomaterials: synthesis and applications in hydrogen evolution reaction, Chem. Soc. Rev. 45 (6) (2016) 1529–1541, https://doi.org/10.1039/C5CS00434A.
[6] D. Kang, T.W. Kim, S.R. Kubota, A.C. Cardiel, H.G. Cha, K.-S. Choi, Electrochemical synthesis of photoelectrodes and catalysts for use in solar water splitting, Chem. Rev. 115 (23) (2015) 12839–12887, https://doi.org/10.1021/acs.chemrev.5b00498.
[7] Y. Bai, K. Hippalgaonkar, R.S. Sprick, Organic materials as photocatalysts for water splitting, J. Mater. Chem. A 9 (30) (2021) 16222–16232, https://doi.org/10.1039/D1TA03710B.
[8] M. Bajdich, M. García-Mota, A. Vojvodic, J.K. Nørskov, A.T. Bell, Theoretical investigation of the activity of cobalt oxides for the electrochemical oxidation of water, J. Am. Chem. Soc. 135 (36) (2013) 13521–13530, https://doi.org/10.1021/ja405997s.
[9] W.M. Haynes, CRC handbook of chemistry and physics, CRC Press, 2014.
[10] S.A. Khalate, S.A. Kadam, Y.-R. Ma, S.S. Pujari, S.J. Marje, P.K. Katkar, A.C. Lokhande, U.M. Patil, Hydrothermally synthesized iron phosphate hydroxide thin film electrocatalyst for electrochemical water splitting, Electrochim. Acta 319 (2019) 118–128, https://doi.org/10.1016/j.electacta.2019.06.162.
[11] L. Cao, Q. Luo, J. Chen, L. Wang, Y. Lin, H. Wang, X. Liu, X. Shen, W. Zhang, W. Liu, Z. Qi, Z. Jiang, J. Yang, T. Yao, Dynamic oxygen adsorption on single-atomic ruthenium catalyst with high performance for acidic oxygen evolution reaction, Nat. Commun. 10 (2019) 1–9, https://doi.org/10.1038/s41467-019-12886-z.
[12] R. Jiang, S. Tung, Z. Tang, L. Li, L. Ding, X. Xi, Y. Liu, L. Zhang, J. Zhang, A review of core-shell nanostructured electrocatalysts for oxygen reduction reaction, Energy Storage Mater. 12 (2018) 260–276, https://doi.org/10.1016/j.ensm.2017.11.005.
[13] S. Siracusano, N. Van Dijk, E. Payne-Johnson, V. Baglio, A.S. Aricò, Nanosized IrO_x and $IrRuO_x$ electrocatalysts for the O_2 evolution reaction in PEM water electrolysers, Appl. Catal. B: Environ. 164 (2015) 488–495, https://doi.org/10.1016/j.apcatb.2014.09.005.
[14] S. Cherevko, S. Geiger, O. Kasian, N. Kulyk, J.P. Grote, A. Savan, B.R. Shrestha, S. Merzlikin, B. Breitbach, A. Ludwig, K.J. Mayrhofer, Oxygen and hydrogen evolution reactions on Ru, RuO_2, Ir, and IrO_2 thin film electrodes in acidic and alkaline electrolytes: A comparative study on activity and stability, Catal. Today 262 (2016) 170–180, https://doi.org/10.1016/j.cattod.2015.08.014.
[15] M.W. Kanan, D.G. Nocera, In situ formation of an oxygen-evolving catalyst in neutral water containing phosphate and Co^{2+}, Science 321 (5892) (2008) 1072–1075.
[16] A. Bergmann, I. Zaharieva, H. Dau, P. Strasser, Electrochemical water splitting by layered and 3D cross-linked manganese oxides: Correlating structural motifs and catalytic activity, Energy Environ. Sci. 6 (2013) 2745–2755, https://doi.org/10.1039/C3EE41194J.
[17] M. Risch, F. Ringleb, M. Kohlhoff, P. Bogdanoff, P. Chernev, I. Zaharieva, H. Dau, Water oxidation by amorphous cobalt-based oxides: In situ tracking of redox transitions and mode of catalysis, Energy Environ. Sci. 8 (2) (2015) 661–674, https://doi.org/10.1039/C4EE03004D.
[18] J. Zhu, L. Hu, P. Zhao, L.Y.S. Lee, K.-Y. Wong, Recent advances in electrocatalytic hydrogen evolution using nanoparticles, Chem. Rev. 120 (2) (2020) 851–918, https://doi.org/10.1021/acs.chemrev.9b00248.
[19] B.S. Yeo, A.T. Bell, Enhanced activity of gold-supported cobalt oxide for the electrochemical evolution of oxygen, J. Am. Chem. Soc. 133 (14) (2011) 5587–5593, https://doi.org/10.1021/ja200559j.
[20] X. Long, J. Li, S. Xiao, K. Yan, Z. Wang, H. Chen, S. Yang, A strongly coupled graphene and FeNi double hydroxide hybrid as an excellent electrocatalyst for the oxygen evolution reaction, Angew. Chem. 126 (29) (2014) 7714–7718, https://doi.org/10.1002/ange.201402822.
[21] V. Di Palma, G. Zafeiropoulos, T. Goldsweer, W.M.M. Kessels, M.C.M. van de Sandena, M. Creatore, M.N. Tsampas, Atomic layer deposition of cobalt phosphate thin films for the oxygen evolution reaction, Electrochem. Commun. 98 (2019) 73–77, https://doi.org/10.1016/j.elecom.2018.11.021.
[22] Y. Wang, B. Kong, D. Zhao, H. Wang, C. Selomulya, Strategies for developing transition metal phosphides as heterogeneous electrocatalysts for water splitting, Nanotoday 15 (2017) 26–55, https://doi.org/10.1016/j.nantod.2017.06.006.
[23] S.J. Marje, P.K. Katkar, S.B. Kale, A.C. Lokhande, C.D. Lokhande, U.M. Patil, Effect of phosphate variation on morphology and electrocatalytic activity (OER) of hydrous nickel pyrophosphate thin films, J. Alloy. Compd. 779 (2019) 49–58, https://doi.org/10.1016/j.jallcom.2018.11.213.
[24] P.K. Katkar, S.J. Marje, S.B. Kale, A.C. Lokhande, C.D. Lokhande, U.M. Patil, Synthesis of hydrous cobalt phosphate electro-catalysts by a facile hydrothermal method for enhanced oxygen evolution reaction: effect of urea variation, CrystEngComm. 21 (5) (2019) 884–893, https://doi.org/10.1039/C8CE01653D.
[25] M. Liu, Z. Qu, D. Yin, X. Chen, Y. Zhang, Y. Guo, D. Xiao, Cobalt−iron pyrophosphate porous nanosheets as highly active electrocatalysts for the oxygen evolution reaction, ChemElectroChem. 5 (1) (2018) 36–43, https://doi.org/10.1002/celc.201700956.
[26] D. Yin, Z. Jin, M. Liu, T. Gao, H. Yuan, D. Xiao, Microwave-assisted synthesis of the cobalt-iron phosphates nanosheets as an efficient electrocatalyst for water oxidation, Electrochim. Acta 260 (2018) 420–429, https://doi.org/10.1016/j.electacta.2017.12.007.
[27] C. Li, X. Mei, F.L.Y. Lam, X. Hu, Amorphous iron and cobalt based phosphate nanosheets supported on Ni foam as superior catalysts for hydrogen evolution reaction, ACS Appl. Energy Mater. 1 (2018) 6764–6768, https://doi.org/10.1021/acsaem.8b01766.
[28] S.A. Khalate, S.A. Kadam, Y.-R. Ma, S.S. Pujari, U.M. Patil, Cobalt doped iron phosphate thin film: An effective catalyst for electrochemical water splitting, J. Alloy. Compd. 885 (2021), https://doi.org/10.1016/j.jallcom.2021.160914 160914.
[29] G. Hodes, Chemical Solution Deposition of Semiconductor Films, Marcel Dekker Inc., New York, CRC Press, 2001.
[30] P.K. Katkar, S.J. Marje, S.S. Pujari, S.A. Khalate, A.C. Lokhande, U.M. Patil, Enhanced energy density of all-solid-state asymmetric supercapacitors based on morphologically tuned hydrous cobalt phosphate electrode as cathode material, ACS Sustainable Chem. Eng. 7 (13) (2019) 11205–11218, https://doi.org/10.1021/acssuschemeng.9b00504.
[31] C. Murugesan, S. Lochab, B. Senthilkumar, P. Barpanda, Earth-abundant alkali iron phosphate ($AFePO_4$) as efficient electrocatalysts for oxygen reduction reaction in alkaline solution, ChemCatChem. 10 (2018) 1122–1127, https://doi.org/10.1002/cctc.201701423.
[32] H.B. Li, M.H. Yu, X.H. Lu, P. Liu, Y. Liang, J. Xiao, Y.X. Tong, G.W. Yang, Amorphous cobalt hydroxide with superior pseudocapacitive performance, ACS Appl. Mater. Interfaces 6 (2) (2014) 745–749, https://doi.org/10.1021/am404769z.
[33] J.B. Condon, Surface Area and Porosity Determinations by Physisorption: Measurements and Theory, 1st ed., Boston, Elsevier, Amsterdam, 2006.
[34] Y. Li, Z. Wang, J. Hu, S. Li, Y. Du, X. Han, P. Xu, Metal-organic frameworks derived interconnected bimetallic metaphosphate nanoarrays for efficient electrocatalytic oxygen evolution, Adv. Funct. Mater. 30 (25) (2020), https://doi.org/10.1002/adfm.201910498 1910498.
[35] S.A. Kadam, G.T. Phan, D.V. Pham, R.A. Patil, C.-C. Lai, Y.-R. Chen, Y. Liou, Y.-R. Ma, Doping-free bandgap tunability in Fe_2O_3 nanostructured films, Nanoscale Adv. 3 (19) (2021) 5581–5588, https://doi.org/10.1039/D1NA00442E.
[36] R. Gresch, W. Müller-Warmuth, H. Dutz, X-ray photoelectron spectroscopy of sodium phosphate glasses, J. Non-Crystalline Solid 34 (1) (1979) 127–136, https://doi.org/10.1016/0022-3093(79)90012-7.
[37] B. Li, Y. Shi, K. Huang, M. Zhao, J. Qiu, H. Xue, H. Pang, Cobalt-doped nickel phosphite for high performance of electrochemical energy storage, Small 14 (13) (2018), https://doi.org/10.1002/smll.201703811 1703811.
[38] H. Dan, K. Tao, Q. Zhou, Y. Gong, J. Lin, Ni-doped cobalt phosphite, $Co_{11}(HPO_3)_8(OH)_6$, with different morphologies grown on Ni foam hydro (solvo)thermally for high-performance supercapacitor, ACS Appl. Mater. Interfaces 10 (37) (2018) 31340–31354, https://doi.org/10.1021/acsami.8b0983610.1021/acsami.8b09836.s001.
[39] C. Chen, N. Zhang, Y. He, B. Liang, R. Ma, X. Liu, Controllable fabrication of amorphous Co-Ni pyrophosphates for tuning electrochemical performance in supercapacitors, ACS Appl. Mater. Interfaces 8 (2016) 23114, https://doi.org/10.1016/j.inoche.2021.108981.
[40] H. Pang, Y.-Z. Zhang, Z. Run, W.-Y. Lai, W. Huang, Amorphous nickel pyrophosphate microstructures for high-performance flexible solid-state electrochemical energy storage devices, Nano Energy 17 (2015) 339–347, https://doi.org/10.1016/j.nanoen.2015.07.030.
[41] S.J. Marje, V.V. Patil, V.G. Parale, H.-H. Park, P.A. Shinde, J.L. Gunjakar, C.D. Lokhande, U.M. Patil, Microsheets like nickel cobalt phosphate thin films as cathode for hybrid asymmetric solid-state supercapacitor: Influence of nickel and cobalt ratio variation, Chem. Eng. J. 429 (2022), https://doi.org/10.1016/j.cej.2021.132184 132184.
[42] C.C.L. McCrory, S. Jung, J.C. Peters, T.F. Jaramillo, Benchmarking heterogeneous electrocatalysts for the oxygen evolution reaction, J. Am. Chem. Soc. 135 (45) (2013) 16977–16987, https://doi.org/10.1021/ja407115p.
[43] B.S. Brunschwig, M.H. Chou, C. Creutz, P. Ghosh, N. Sutin, Mechanisms of water oxidation to oxygen: cobalt (IV) as an intermediate in the aquocobalt (II)-catalyzed reaction, J. Am. Chem. Soc. 105 (14) (1983) 4832–4833, https://doi.org/10.1021/ja00352a050.